

# Spiral-wave dynamics in a mathematical model of human ventricular tissue with myocytes and Purkinje fibers

Alok Ranjan Nayak,<sup>1,\*</sup> A. V. Panfilov,<sup>2,3</sup> and Rahul Pandit<sup>4,†</sup>

<sup>1</sup>*International Institute of Information Technology (IIIT-Bhubaneswar), Gothapatna, Po: Malipada, Bhubaneswar 751003, India*

<sup>2</sup>*Department of Physics and Astronomy, Gent University, Krijgslaan 281, S9, 9000 Gent, Belgium*

<sup>3</sup>*Moscow Institute of Physics and Technology (State University), Dolgoprudny, Moscow Region, Russia*

<sup>4</sup>*Centre for Condensed Matter Theory, Department of Physics, Indian Institute of Science, Bangalore 560012, India*

(Received 23 June 2016; revised manuscript received 18 October 2016; published 13 February 2017)

We present systematic numerical studies of the possible effects of the coupling of human endocardial and Purkinje cells at cellular and two-dimensional tissue levels. We find that the autorhythmic-activity frequency of the Purkinje cell in a composite decreases with an increase in the coupling strength; this can even eliminate the autorhythmicity. We observe a delay between the beginning of the action potentials of endocardial and Purkinje cells in a composite; such a delay increases as we decrease the diffusive coupling, and eventually a failure of transmission occurs. An increase in the diffusive coupling decreases the slope of the action-potential-duration-restitution curve of an endocardial cell in a composite. By using a minimal model for the Purkinje network, in which we have a two-dimensional, bilayer tissue, with a layer of Purkinje cells on top of a layer of endocardial cells, we can stabilize spiral-wave turbulence; however, for a sparse distribution of Purkinje-ventricular junctions, at which these two layers are coupled, we can also obtain additional focal activity and many complex transient regimes. We also present additional effects resulting from the coupling of Purkinje and endocardial layers and discuss the relation of our results to the studies performed in anatomically accurate models of the Purkinje network.

DOI: [10.1103/PhysRevE.95.022405](https://doi.org/10.1103/PhysRevE.95.022405)

## I. INTRODUCTION

Spiral waves form and propagate in many excitable media that include systems with chemical oscillations [1,2], catalysts on surfaces, for instance, the oxidation of carbon monoxide on a platinum surface [3,4], and, most important, cardiac tissue [5,6]. Such spiral waves in cardiac tissue play an important role in life-threatening cardiac arrhythmias like ventricular tachycardia and ventricular fibrillation, which are often associated, respectively, with an unbroken spiral wave and broken spiral waves of electrical activation in cardiac tissue [7,8]. Several experimental studies have shown that the dynamics of cardiac arrhythmias depends not only on wave propagation in the myocardium, but it is also substantially affected by wave propagation through the Purkinje network [9]. However, in experimental studies, the mechanisms of such influence have neither been clearly identified nor studied, because of the difficulty in varying parameters like the Purkinje-myocardium coupling. Therefore, the application of alternative methods, such as mathematical modeling, to this problem is of great interest. In this paper, we study the possible effects of the coupling of human endocardial and Purkinje cells, at both cellular and two-dimensional tissue levels, by using detailed ionic models for such cells, and a *minimal model* for the Purkinje-fiber network; this minimal model allows us to explore in detail the dependence of spiral-wave dynamics, in both endocardial and Purkinje layers,

on the density of Purkinje-ventricular junctions, at which the Purkinje and endocardial layers are connected in our model. We show how such couplings, tissue properties, and the architecture of Purkinje fibers affect spiral-wave dynamics by using spatiotemporal-chaos theory, nonlinear dynamics, and cardiac biophysics. As in many nonlinear systems, our studies show that spiral-wave dynamics depends sensitively on endocardial cell parameters, the endocardial and Purkinje coupling, and the spatial distribution of Purkinje-ventricular junctions.

This paper proceeds as follows: In Sec. II we formulate our endocardial and Purkinje model, first for a single, composite, cell and then for two-dimensional tissue; we then give an overview of our numerical scheme. In Sec. III we present our numerical studies of spiral-wave dynamics in the endocardial and Purkinje tissue model. We end with a discussion of our results in Sec. IV.

## II. MODEL

When an endocardial cell and a Purkinje cell in a composite are coupled, via a heterocellular coupling [10,11], at a Purkinje-ventricular junction site with strength  $\kappa$ , the transmembrane potentials  $V_e$  and  $V_p$  for the endocardial and Purkinje cells, respectively, obey the following ordinary differential equations:

$$\frac{dV_e}{dt} = -I_{\text{ion},e} - \kappa(V_e - V_p), \quad (1)$$

$$\frac{dV_p}{dt} = -I_{\text{ion},p} + \kappa(V_e - V_p), \quad (2)$$

\*Formerly at Robert Bosch Centre for Cyber Physical Systems, Division of Interdisciplinary Research, Indian Institute of Science, Bangalore 560012, India; aloknayak@iiit-bh.ac.in

†rahul@physics.iisc.ernet.in

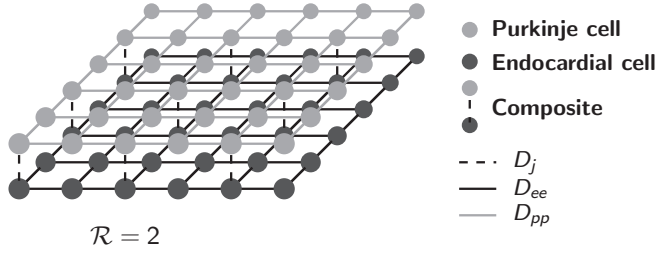


FIG. 1. Schematic diagram of a small part of our square simulation domain consisting of endocardial and Purkinje cells with  $\mathcal{R} = 2$ ; here  $\mathcal{R}^2$  is the ratio of the total number of the endocardial (or Purkinje) cells to the total number of sites where the Purkinje cells are coupled to the endocardial cells. If  $\mathcal{R} = 1$ , then every Purkinje cell is connected directly to the endocardial cell below it. The abbreviations  $D_{ee}$ ,  $D_{pp}$ , and  $D_j$  stand for diffusion constant in the endocardial layer, diffusion constant in the Purkinje layer, and coupling strength between an endocardial cell and a Purkinje cell in our bilayer domain.

where  $\kappa = D_j/\Delta z^2$  provides the coupling strength between endocardial and Purkinje cells with  $D_j$  the gap-junctional diffusible coupling between these two cells [10,11];  $D_j$  and  $\Delta z$  are measured in  $\text{mm}^2/\text{ms}$  and  $\text{mm}$ , respectively. All the ionic currents are normalized per unit capacitance, which is, in our models, the same for the myocytes and the Purkinje cells [12,13].

We use biophysically realistic ionic models for human endocardial and Purkinje cells. In particular, we use (a) the ventricular model developed by ten Tusscher *et al.* (the TP06 model) [12], and (b) the Purkinje model developed by Stewart *et al.* [13]. The equations for these models, including the ordinary differential equations for the ion-channel gating variables and the ion dynamics, are given in Refs. [12,13].

In our two-dimensional (2D) model, we arrange Purkinje fibers in a sheet [14,15] that lies on top of a layer of endocardial cells. We allow the Purkinje cells in the top layer to be connected to the endocardial cells in the bottom layer at a fraction  $1/\mathcal{R}^2$  of the total number of sites. The connections between endocardial and Purkinje cells are at periodically spaced points in our simulation domain; these points are the analogs of Purkinje-ventricular junctions in our mathematical model;  $\mathcal{R}^2$  is the ratio of the total number of sites to the number of Purkinje-ventricular junctions: it measures the density of Purkinje-ventricular junctions in the domain. Figure 1 shows a schematic diagram of a portion of our endocardial and Purkinje composite bilayer with  $\mathcal{R} = 2$ . Our 2D, composite, bilayer-tissue model can be thought of as a very simple approximation for endocardial tissue with Purkinje fibers embedded on its surface. The simplicity of our model allows us to examine the dynamics of spiral waves in much greater detail than has been attempted so far in any mathematical model for ventricular tissue with Purkinje fibers.

The transmembrane potentials  $V_e$  and  $V_p$  of endocardial and Purkinje cells, respectively, for such a 2D bilayer domain can be modeled by the following *discrete-reaction-diffusion*

TABLE I. Parameter sets  $\mathcal{P}1$ ,  $\mathcal{P}2$ , and  $\mathcal{P}3$  for an endocardial cell in our model; here,  $\sigma_f$  is the scale factor of the time constant  $\tau_f$ . The remaining model parameters are the same as in their parent model [12].

Parameter sets	$G_{Na}$ (nS/pF)	$G_{Kr}$ (nS/pF)	$G_{Ks}$ (nS/pF)	$G_{pCa}$ (nS/pF)	$G_{pK}$ (nS/pF)	$\sigma_f$
$\mathcal{P}1$	14.838	0.172	0.441	0.8666	0.00219	2
$\mathcal{P}2$	$5 \times 14.838$	0.153	0.392	0.1238	0.0146	1
$\mathcal{P}3$	14.838	0.153	0.392	0.1238	0.0146	1

equations [16,17]:

$$\begin{aligned} \frac{\partial V_e(i,k)}{\partial t} = & -I_{\text{ion},e}(i,k) - \frac{D_j(i,k)}{(\Delta z)^2} [V_e(i,k) - V_p(i,k)] \\ & + \frac{D_{ee}}{(\Delta x)^2} [V_e(i+1,k) - 2V_e(i,k) + V_e(i-1,k)] \\ & + \frac{D_{ee}}{(\Delta y)^2} [V_e(i,k+1) - 2V_e(i,k) + V_e(i,k-1)], \end{aligned} \quad (3)$$

$$\begin{aligned} \frac{\partial V_p(i,k)}{\partial t} = & -I_{\text{ion},p}(i,k) + \frac{D_j(i,k)}{(\Delta z)^2} [V_e(i,k) - V_p(i,k)] \\ & + \frac{D_{pp}}{(\Delta x)^2} [V_p(i+1,k) - 2V_p(i,k) + V_p(i-1,k)] \\ & + \frac{D_{pp}}{(\Delta y)^2} [V_p(i,k+1) - 2V_p(i,k) + V_p(i,k-1)], \end{aligned} \quad (4)$$

where  $D_{ee}$  and  $D_{pp}$  represent, respectively, diffusion constants in the endocardial and Purkinje layers.  $D_j(i,k)$  represents coupling between endocardial and Purkinje cells in the bilayer tissue. At points, in the bilayer tissue, where an endocardial cell and a Purkinje cell are coupled to each other, its value is equal to a constant  $D_j(i,k) = D_j$ , which is a parameter that we vary in our simulations as we specify below; these coupling points are periodically spaced in our simulation domain and at these points both  $i$  and  $k$  are divisible by  $\mathcal{R}$ ; at all other points  $D_j(i,k) = 0$  (Fig. 1).

We use a 2D square domain consisting of two layers with  $1024 \times 1024$  grid points and lattice spacing  $\Delta x = \Delta y = 0.25$  mm, so the side of each square domain is  $L = 256$  mm; one of these layers contains endocardial cells and the other Purkinje cells. These two layers are separated by a distance  $\Delta z = 0.25$  mm. We use a forward-Euler method for the time evolution of the transmembrane potentials with a time step  $\Delta t = 0.02$  ms. We use Neumann (*no-flux*) boundary conditions.

In our studies, we use three parameter sets  $\mathcal{P}1$ ,  $\mathcal{P}2$ , and  $\mathcal{P}3$  (Table I), which yield breakup, pre-breakup, and stable spiral rotation, respectively, in our 2D endocardial layer (see below for details). For these studies, we vary the *time constant*,  $\tau_f$ , for the  $f$  gate and the following five ionic conductances for the endocardial cell [12]; these are (a)  $G_{Na}$  for the fast  $Na^+$  current,  $I_{Na}$ , (b)  $G_{Kr}$ , related to the rapid-delayed rectifier current of  $K^+$ , namely,  $I_{Kr}$ , (c)  $G_{Ks}$ , related to the slow-delayed rectifier current of  $K^+$ , namely,  $I_{Ks}$ , (d)  $G_{pCa}$  for the plateau  $Ca^{2+}$  current,  $I_{pCa}$ , and (e)  $G_{pK}$  for the plateau

$K^+$  current,  $I_{pK}$ . The changes of conductances are related to the variation of physiological conditions caused because of either diseases or the effects of the drugs; and the variation of  $\tau_f$  is acceptable because it is related with the calcium concentration that can be controlled by ryanodine as suggested in Refs. [18,19].

The heterocellular, myocyte-Purkinje, coupling is always lower than its homocellular counterparts (i.e., myocyte-myocyte and Purkinje-Purkinje diffusive couplings); in particular, Ref. [20] uses a value for  $D_j$  that is about 6% of the homocellular coupling. Therefore, we perform simulations by varying  $D_j$  in the range  $0 < D_j \leq 0.1D_{ee}$ , where  $D_{ee} = 0.154 \text{ mm}^2/\text{ms}$  represents the diffusive coupling between endocardial cells [12].

We use the S1-S2 cross-field protocol [21] to initiate spiral waves in a square simulation domain of side  $L = 256 \text{ mm}$ . In this protocol, we apply S1 and S2 stimuli with strengths  $150 \text{ pA/pF}$  for 3 ms.

To characterize the spiral state in the endocardial layer, we record the time series of  $V_e(x,y,t)$  from 25 sites in the endocardial simulation domain. For the power spectra  $E(\omega)$  of these time series, we use the last  $2 \times 10^5$  data points out of  $4 \times 10^5$  data points to eliminate transients. The final state of the endocardial layer is decided by analyzing these power spectra and the spatiotemporal evolution of  $V_e$ .

### III. RESULTS

We first describe our results for a composite endocardial-Purkinje cell and then for spiral-wave dynamics in 2D square domain.

#### A. A composite with an endocardial and a Purkinje cell

Purkinje cells can display autorhythmicity [9] when the sinoatrial node fails to fire action potentials; occasionally, premature impulses can be transmitted to the ventricles by Purkinje fibers if a conduction delay occurs in the atrioventricular node. A Purkinje cell can fire action potential between 15 and 40 times per minute [22]. Therefore, we have carried out simulations to examine how the autorhythmic activity of a Purkinje cell changes, in our composite model described by Eqs. (1) and (2) in Sec. II, as a function of the coupling strength  $D_j$  between the endocardial and Purkinje cells. In Fig. 2 we show autorhythmic-activity dynamics of a Purkinje cell in a composite; here squares (■) and triangles (▲) represent coupled Purkinje cells with  $D_j = 0.001D_{ee}$  and  $D_j = 0.003D_{ee}$ , respectively, and circles (●) are for an uncoupled Purkinje cell. Figure 2(a) shows plots of the Purkinje transmembrane potential  $V_p$  in a composite. We see that, at a coupling of  $D_j = 0.001D_{ee}$ , the frequency of autorhythmic activity decreases; and at  $D_j = 0.003D_{ee}$  it is eliminated. The mechanism behind this effect is illustrated in Fig. 2(b), which shows the current  $\kappa(V_e - V_p)$  between endocardial and Purkinje cells. We see that this current is negative and the endocardial cell in this composite acts like a current sink. An increase in the coupling  $D_j$  increases this sink effect, and, at  $D_j = 0.003D_{ee}$ , it eliminates autorhythmic activity. Figure 2(c) shows the dependence of the frequency  $f$  of the autorhythmic activity on the coupling  $D_j^{\text{norm}} = D_j/D_{ee}$ . We observe that  $f$  decreases as  $D_j$  increases and, finally, the

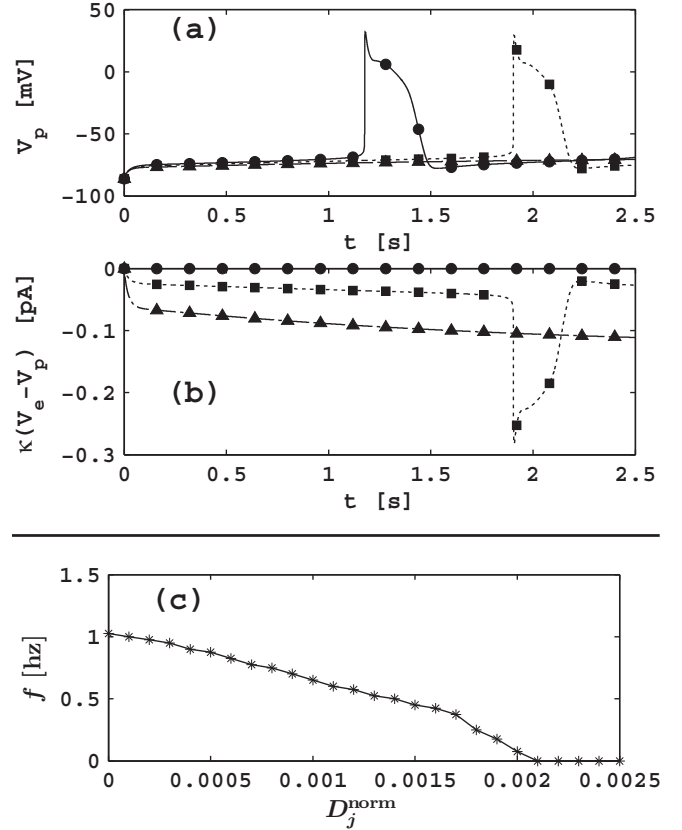


FIG. 2. Autorhythmic activity of a Purkinje cell in an endocardial-Purkinje composite; here squares (■) and triangles (▲) represent coupled Purkinje cells with  $D_j = 0.001D_{ee}$  and  $D_j = 0.003D_{ee}$ , respectively, and circles (●) denote data points from an uncoupled Purkinje cell. (a) Plots of the Purkinje action potential  $V_p$  in a composite. (b) Plots of the current  $\kappa(V_e - V_p)$  between endocardial and Purkinje cells; such plots show that the endocardial cell in this composite acts like a current sink. (c) Plots of the frequency  $f$  of the autorhythmic activity of the Purkinje cell in a composite versus the coupling  $D_j^{\text{norm}} = D_j/D_{ee}$ . Note that  $f$  decreases as  $D_j$  increases, and, finally, autorhythmicity is eliminated after  $D_j \simeq 0.0021D_{ee}$ .

Purkinje cell in a composite loses its autorhythmic activity after  $D_j \simeq 0.0021D_{ee}$ .

We study the action-potential behaviors of endocardial and Purkinje cells in a composite by exciting (1) an endocardial cell and (2) a Purkinje cell, as investigated by Huelsing *et al.* [10,11] in their *in vitro* studies on a rabbit Purkinje cell, which they couple to a ventricular myocyte by an electronic circuit. To initiate action potentials, we apply a current pulse of strength  $52 \text{ pA/pF}$  to one of the cells of the composite or both for 3 ms. We also compute the conduction-delay time ( $\Delta t$ ) from the endocardial to the Purkinje cell, or vice versa, during the onset of such action potentials. Figure 3(a) shows plots of the Purkinje action potential  $V_p$  and the endocardial action potential  $V_e$  when the stimulus is applied to the endocardial cell with  $D_j = 0.01D_{ee}$  (■, □). We also compare action potentials in uncoupled cells  $D_j = 0$  (●, ○). Figure 3(b) shows the same plot when the stimulus is applied to the Purkinje cell. In all cases, we find a delay between the excitation of the cells. However, for endocardial stimulation, this delay is

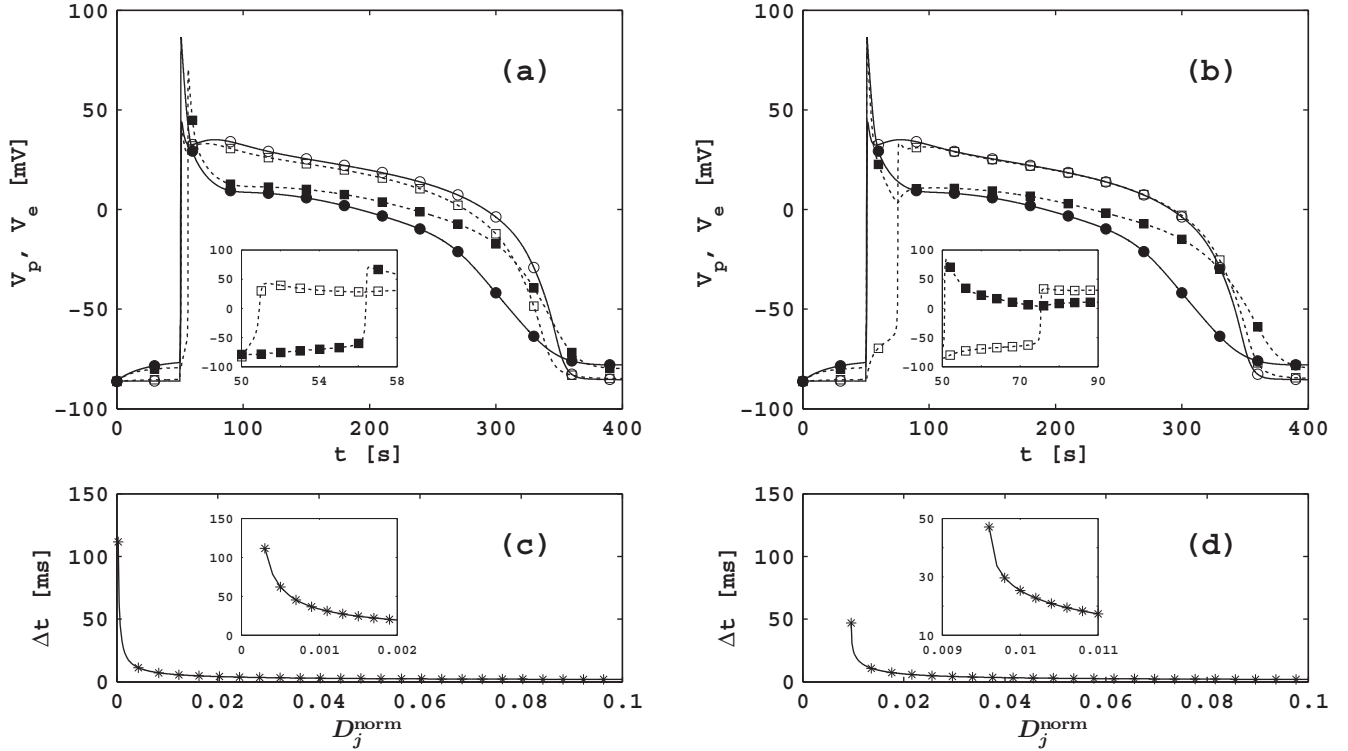


FIG. 3. Action potentials for endocardial and Purkinje cells in a composite and their conduction-delay times  $\Delta t$ . (a) Plots of the action potentials  $V_p$  (● or ■) and  $V_e$  (○ or □), when a stimulus is applied to both uncoupled endocardial and Purkinje cells, i.e.,  $D_j = 0$  (●, ○) and the endocardial cell in our composite with  $D_j = 0.01 D_{ee}$  (■, □). (b) Plots as in (a), but with a stimulus applied to the Purkinje cell in our composite. Insets in (a) and (b) show the depolarization phases of action potentials on an expanded scale; these inset plots show the conduction delay from an endocardial to a Purkinje cell, or vice versa, depending on whether the stimulus is applied to an endocardial cell or to a Purkinje cell in a composite. Such inset plots show that, for a given value of  $D_j$ , the conduction delay time is more when the stimulus is applied to the Purkinje cell than when it is applied to the endocardial cell in a composite. (c) Plots of the conduction-delay time  $\Delta t$  from the endocardial to the Purkinje cells versus  $D_j^{\text{norm}} = D_j/D_{ee}$ , when the stimulus is applied to the endocardial cell of a composite. (d) Plots as in (c) but of the conduction delay from the Purkinje to the endocardial cell, when the stimulus is applied to the Purkinje cell of a composite. Insets in (c) and (d) show the plots of such delay on an expanded time scale; these insets also show that, as we decrease  $D_j$ , the failure of the initiation of the action potential in a Purkinje cell, when the stimulus is applied to the endocardial cell in a composite, occurs earlier than it does when the stimulus is applied to the Purkinje cell in a composite.

substantially smaller. Such asymmetry in the delay arises because of the different physiological properties of endocardial and Purkinje cells; in particular, the threshold of a Purkinje cell is lower than that of an endocardial cell, as suggested by Huelsing *et al.* [10]. This delay as a function of the coupling strength  $D_j^{\text{norm}} = D_j/D_{ee}$  is shown in Fig. 3(c) for epicardial stimulation and in Fig. 3(d) for Purkinje-cell stimulation. Insets show the plots on an expanded time scale. We see that not only are the delays with Purkinje stimulation larger than those with endocardial stimulation, but also the failure of transmission occurs more easily for the case of Purkinje stimulation. Our results on delays and the propagation block of the AP are in qualitative agreement with those of Huelsing *et al.* [10] and ten Tusscher *et al.* [23].

The restitution of the action potential duration plays an important role in the stability of spiral waves [24–26]. It has been shown, in both experimental and numerical studies [24–27], that a steep slope of the action-potential-duration-restitution (APDR) curve, a plot of the action potential duration (APD) versus the diastolic interval (DI), leads to spiral-wave instability. Therefore, we carry out a set of simulations to

obtain such a plot for the endocardial cell in a composite for different values of the coupling strength  $D_j$  (Fig. 4) for three parameter sets  $\mathcal{P}1$ ,  $\mathcal{P}2$ , and  $\mathcal{P}3$ , which we use later to study spiral-wave dynamics in two dimensions, corresponding to breakup, prebreakup, and a stable spiral, respectively. We see that for all parameter sets, represented in Figs. 4(a)–4(c), coupling to the Purkinje cell decreases the slope of the restitution curve. Therefore, we expect that spiral-wave dynamics in the endocardial layer can be stabilized by the inclusion of Purkinje fibers. However, this dependence is not monotonic: for strong coupling (▲)  $D_j = 0.1 D_{ee}$ , the slope is less steep than for intermediate coupling (■)  $D_j = 0.01 D_{ee}$ , as compared with an uncoupled endocardial cell (●).

## B. Wave dynamics in a two-dimensional domain

Before we start our investigation of spiral-wave dynamics in bilayers, we present, for subsequent comparisons, spiral waves in isolated endocardial and Purkinje layers. In Figs. 5(a)–5(c) we show pseudocolor plots of the endocardial transmembrane potential  $V_e$ , in a 2D domain, for the parameter sets  $\mathcal{P}1$ ,  $\mathcal{P}2$ ,



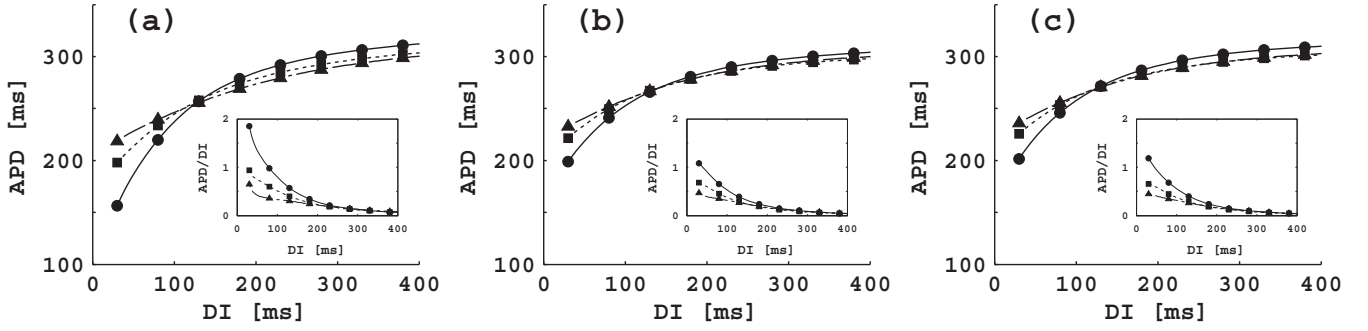


FIG. 4. Action potential duration restitution (APDR) and its slope for an endocardial cell in a composite with different sets of endocardial parameters; here circles ( $\bullet$ ) represent an uncoupled endocardial cell, and squares ( $\blacksquare$ ) and triangles ( $\blacktriangle$ ) are used, respectively, for an endocardial cell in a composite with  $D_j = 0.01D_{ee}$  and  $D_j = 0.1D_{ee}$ . The plots in (a), (b), and (c) show the APDR for parameter sets  $\mathcal{P}1$ ,  $\mathcal{P}2$ , and  $\mathcal{P}3$  (see Table I), respectively; inset plots show the slopes of the APDR curve. The steepness of the APDR curve decreases, for all the parameter sets, as we increase  $D_j$  in a composite. The maximum slopes of the APDR are  $\simeq 2.0$ ,  $\simeq 1.1$ , and  $\simeq 1.1$ , for an uncoupled endocardial cell ( $\bullet$ ) with parameter sets  $\mathcal{P}1$ ,  $\mathcal{P}2$ , and  $\mathcal{P}3$ , respectively; however, the maximum slope of the APDR for an endocardial cell in a composite decreases as  $D_j$  increases ( $\blacksquare$ ,  $\blacktriangle$ ) because of the coupling to the Purkinje cell.

and  $\mathcal{P}3$ , respectively; and in Fig. 5(d), we show pseudocolor plot of the transmembrane potential of the Purkinje layer  $V_p$  for the diffusive coupling  $D_{pp} = 3D_{ee}$ . Such a threefold increment in Purkinje diffusion coefficient gives a biophysically

reasonable value of conduction velocity,  $CV \simeq 2.1$  mm/ms, in the Purkinje fibers as suggested in Refs. [28,29]. In Figs. 5(e)–5(g) we show, respectively, the time series for the parameter sets  $\mathcal{P}1$ ,  $\mathcal{P}2$ , and  $\mathcal{P}3$ , recorded from a representative

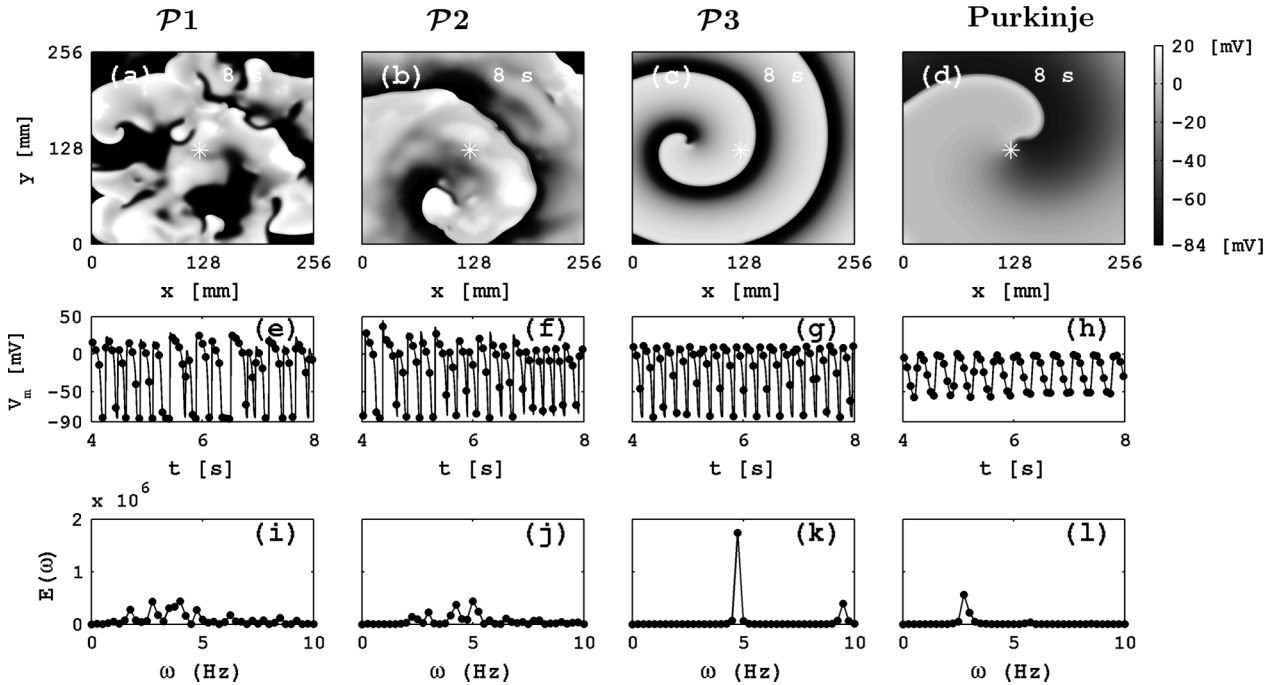


FIG. 5. Spiral-waves dynamics in isolated endocardial and Purkinje 2D simulation domains. Pseudocolor plots of the transmembrane potential  $V_m$  for the endocardial layer with parameter sets (a)  $\mathcal{P}1$ , (b)  $\mathcal{P}2$ , and (c)  $\mathcal{P}3$ , and (d) the Purkinje layer. Panels (e), (f), and (g) show, respectively, the time series for the parameter sets  $\mathcal{P}1$ ,  $\mathcal{P}2$ , and  $\mathcal{P}3$ , recorded from a representative point ( $x = 125$  mm,  $y = 125$  mm) that is marked by an asterisk in (a), (b), and (c); (h) the time series recorded from Purkinje layer, marked by an asterisk in (d). (i), (j), (k), and (l) show power spectra calculated by using these time series (see Methods for the lengths of time series). The irregular time series in (e) and the broad-band nature of the power spectrum in (i) are characteristic of a spiral-turbulence (ST) state in the endocardial layer with the parameter set  $\mathcal{P}1$ ; the pseudocolor plot in (a) shows that this ST state is maintained by multiple waves, i.e., it is a multiple-spiral-turbulence (MST) state. For the parameter set  $\mathcal{P}2$ , the irregular time series in (f) and the development of subsidiary peaks in  $E(\omega)$  in (j) confirm that the temporal evolution of the state is chaotic; the pseudocolor plot in (b) shows the existence of single, meandering, spiral turbulence (SMST), in which the spiral arms and core evolve chaotically in space and time. The pseudocolor plot in (c) shows a rotating spiral (RS) for the parameter set  $\mathcal{P}3$ ; the periodic time series in (g) and the discrete, strong peaks in  $E(\omega)$  at 4.75 Hz and its harmonics in (k) provide evidence of a single-rotating-spiral-periodically (SRSP) for the parameter set  $\mathcal{P}1$ . The pseudocolor plot in (d), the periodic time series in (h), and discrete peaks in the power spectrum, with fundamental frequency  $\omega_f \simeq 2.75$  Hz in (l), show the existence of an SRSP in the Purkinje layer.

point ( $x = 125$  mm,  $y = 125$  mm), marked by asterisks in Figs. 5(a)–5(c); and in Fig. 5(h) we show the time series of  $V_p(x, y, t)$ . In Figs. 5(i)–5(l) we show plots of the power spectra  $E(\omega)$ , which we have obtained from the local time series of  $V_m$ . The irregular time series in Fig. 5(e) and the broad-band nature of the power spectrum in Fig. 5(i) are characteristic of a spiral-turbulence (ST) state in the endocardial layer with the parameter set  $\mathcal{P}1$ ; the pseudocolor plot in Fig. 5(a) shows that this ST state is maintained by multiple waves, so we refer to it as a multiple-spiral-turbulence (MST) state. For the parameter set  $\mathcal{P}2$ , the irregular time series in Fig. 5(f) and broad-band nature of the power spectrum in Fig. 5(j) confirm that the temporal evolution of the state is chaotic; the pseudocolor plot in Fig. 5(b) shows the existence of single, meandering, spiral, in which the spiral arms and core evolve chaotically in space and time; therefore, we call this a single-meandering-spiral-turbulence (SMST) state. For the parameter set  $\mathcal{P}3$ , the plot of  $V_e$  in Fig. 5(c) shows a single, rotating spiral; the periodic nature of the time series in Fig. 5(g) and the discrete, strong peaks in  $E(\omega)$  at the fundamental frequency  $\omega_f = 4.75$  Hz and its harmonics in Fig. 5(k) provide additional evidence for the periodic motion of this spiral wave; therefore, we refer to this as a single-rotating-spiral-periodically (SRSP) state. The pseudocolor plot in Fig. 5(d) shows the existence of a rotating spiral in an isolated Purkinje layer. The power spectrum  $E(\omega)$  in Fig. 5(l) has discrete peaks at the fundamental frequency  $\omega_f = 2.75$  Hz and its harmonics. The resulting periodic time series [Fig. 5(h)] and the discrete peaks in the power spectrum give additional evidence for the existence of an SRSP state in an isolated Purkinje layer.

We now carry out a set of simulations to study the spatiotemporal evolutions of spiral waves, for the parameter sets  $\mathcal{P}1$ ,  $\mathcal{P}2$ , and  $\mathcal{P}3$ , when an endocardial layer is coupled with a Purkinje layer, with  $D_j$  and  $\mathcal{R}$  in the ranges mentioned above. We obtain spiral waves in our composite bilayer by using the S1–S2 protocol in the endocardial layer.

In Figs. 6(a)–6(c) we show, respectively, pseudocolor plots of  $V_e$  in the endocardial layer for the parameter set  $\mathcal{P}1$  with  $D_j = 0.1D_{ee}$  and  $\mathcal{R} = 1, 2$ , and 4; similar plots are shown in Figs. 6(d)–6(f) for  $V_p$  in the Purkinje layer. These pseudocolor plots of  $V_e$  show the existence of an SRSP state in the endocardial layer of our composite bilayer for  $\mathcal{R} = 1$  [Fig. 6(a)] and  $\mathcal{R} = 2$  [Fig. 6(b)]; however, for  $\mathcal{R} = 4$ , we observe a state with spiral absorption (SA) in the endocardial layer of this composite bilayer [Fig. 6(c)]. In the absence of a Purkinje layer, an isolated endocardial layer with the parameter set  $\mathcal{P}1$  displays an MST state as shown in Fig. 5(a). An MST-SRS transitions occurs, in the presence of a Purkinje layer, because of the suppression of the steep slope of the APDR of a myocyte in a composite [see Fig. 4(a)]. We record the local time series for  $V_e$  and  $V_p$  from the representative points, in both endocardial and Purkinje layers, marked by asterisks in Figs. 6(a)–6(f); in Figs. 6(g)–6(i), we show these time series for  $V_e$  (●) and  $V_p$  (○), which lead to the plots of  $E(\omega)$  versus  $\omega$  shown by ● (endocardial layer) and ○ (Purkinje layer) in Figs. 6(j)–6(k). The plots of the time series, in Figs. 6(g)–6(h), and power spectra, in Figs. 6(j)–6(k), show the existence of a single-rotating-spiral state in both endocardial and Purkinje layers; the estimated fundamental

frequencies in both types of layers are  $\omega_e = \omega_p \simeq 4.75$  Hz and  $\omega_e = \omega_p \simeq 4.75$  Hz for  $\mathcal{R} = 1$  and 2, respectively. Two features are worth noting here: (1) the time series of  $V_e$  and  $V_p$  display synchrony, insofar as they show a train of action potentials that are in phase in the two layers, and (2) the width of the spiral-wave arms decreases as  $\mathcal{R}$  increases. For  $\mathcal{R} = 4$ , we observe an SA state in both endocardial and Purkinje layers of our bilayer as shown in the pseudocolor plots in Figs. 6(c) and 6(f). The time series in Fig. 6(i) shows additional evidence for the disappearance of spiral waves in both the endocardial and Purkinje layers simultaneously at time  $t \simeq 5.7$  s. Such an ST state is observed because of the termination of a single, nonstationary spiral, whose core is not stable, by collision with one of the boundaries of the domain. However, for the same parameter set, we may not observe an SA state if we alter the spiral initiation process by changing the timing of the S2 stimulus in the S1–S2 protocol. Note that an MST state in an isolated endocardial layer [cf. Fig. 5(a)] is converted to an SRSP or an SA state by the inclusion of Purkinje cells.

In Fig. 7 we show the counterpart of Fig. 6 for  $\mathcal{R} = 8, 16$ , and 32 and the parameter set  $\mathcal{P}1$ . In the left panel of Fig. 7, we show the pseudocolor plots of  $V_e$  [Fig. 7(a)] and  $V_p$  [Fig. 7(d)], the local time series [Fig. 7(g)], and the power spectrum [Fig. 7(j)] for the parameter set  $\mathcal{P}1$  and  $\mathcal{R} = 8$ . The irregular time series of  $V_e$  (●) in Fig. 7(g) and the broad-band nature of the power spectra (●) in Fig. 7(j) show that the temporal evolution of  $V_e$  is chaotic. Therefore, we confirm the presence of an MST in the endocardial layer of the bilayer, as shown by the pseudocolor plot in Fig. 7(a). Note that an MST state in an isolated layer still remains in the MST state on the inclusion of Purkinje system; this is because of the sparse distribution of connectivity (large  $\mathcal{R}$ ) between the endocardial and Purkinje layers of our bilayer. However, Fig. 7(d) shows that the Purkinje layer displays *periodic* focal-wave activity, because of an MST state in the endocardial layer of the bilayer. The time series of  $V_p$  (○) in Fig. 7(g) and the power spectra (○) in Fig. 7(j) show additional evidence of such periodic wave activity in the Purkinje layer. We find that the frequency of such periodic focal-wave activity is  $\omega_p \simeq 2.35$  Hz; this frequency is close to its value in an uncoupled Purkinje layer [see Fig. 5(l)]. Plots similar to those in the left panel of Fig. 7, for  $\mathcal{P}3$  with  $\mathcal{R} = 16$  and  $\mathcal{R} = 32$ , are shown, respectively, in the middle and right panels of Fig. 7. The pseudocolor plots in Figs. 7(b) and 7(c), the local time series of  $V_e$  (●) in Figs. 7(h) and 7(i), and the power spectra of this time series in Figs. 7(k) and 7(l) show that the spiral state in the endocardial layer of the bilayer is an MST state. However, we still see periodic focal-wave activity in the Purkinje layer of the bilayer as shown in the pseudocolor plots in the Figs. 7(e) and 7(f), the periodic time series of  $V_p$  (○) in Figs. 7(h) and 7(i), and discrete peaks in the power spectra (○) in Figs. 7(k) and 7(l). We estimate the fundamental frequencies for the focal-wave activity in the Purkinje layer of the bilayer are  $\omega_p \simeq 2.0$  Hz and  $\omega_p \simeq 1.5$  Hz for  $\mathcal{R} = 16$  and 32, respectively. Note that the focal-wave frequency decreases as  $\mathcal{R}$  increases, as shown by the power spectra in Figs. 7(j)–7(l) (○). Furthermore, note that an MST state in an isolated layer with  $\mathcal{R} \geq 8$  still remains in the MST state on the inclusion of the Purkinje system.

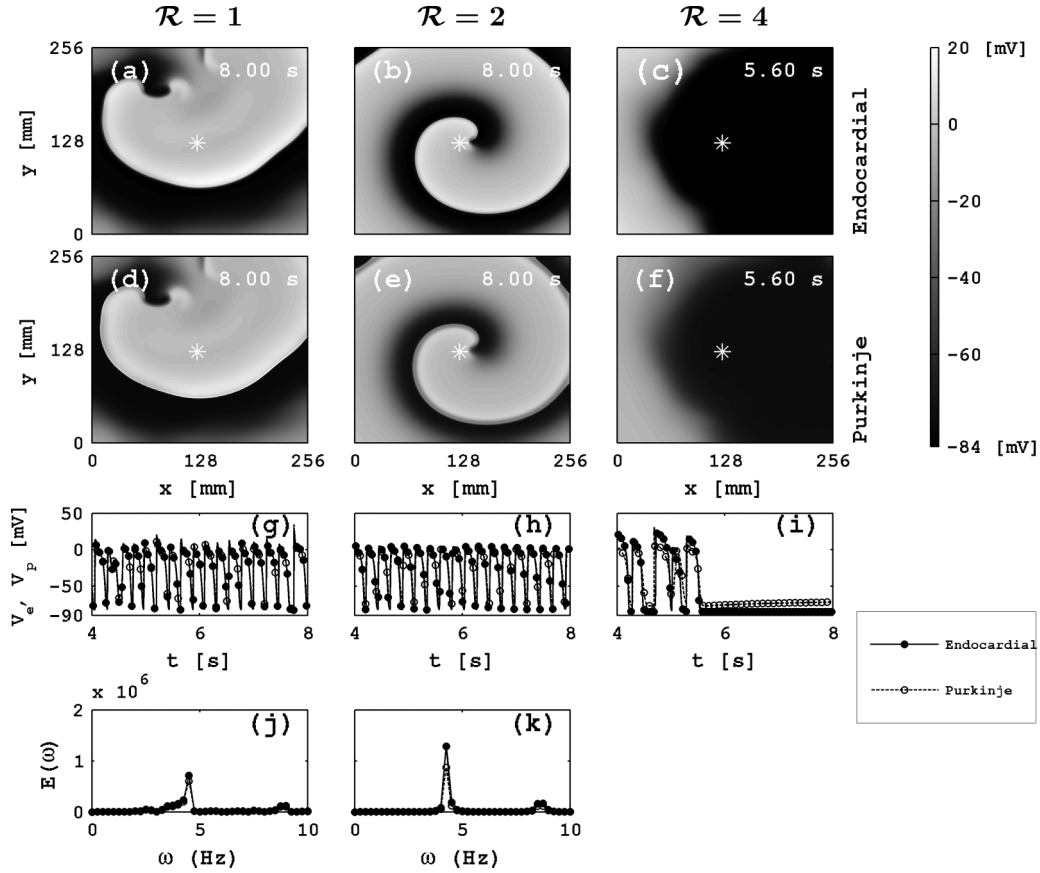


FIG. 6. Spiral-wave dynamics in our composite bilayer for the  $\mathcal{P}1$  parameter set for the endocardial cells with  $D_j = 0.1D_{ee}$  and  $\mathcal{R} = 1$  (left column),  $\mathcal{R} = 2$  (middle column), and  $\mathcal{R} = 4$  (right column). The first row shows pseudocolor plots of the endocardial layer transmembrane potential  $V_e$ ; the plots in the second row are the exact analogs of these for the Purkinje-layer transmembrane potential  $V_p$ . The third row shows plots of the time series for  $V_e$  (●) and  $V_p$  (○), which are recorded from the representative points ( $x = 125$  mm,  $y = 125$  mm), in both endocardial and Purkinje layers; these are marked by asterisks in (a) to (f). The fourth row shows plots of the power spectra  $E(\omega)$  versus the frequency  $\omega$  for the endocardial layer (●) and the Purkinje layer (○). A multiple-spiral-turbulence (MST) state in an isolated endocardial layer [Fig. 5(a)] is converted to a single-rotating-spiral-periodic (SRSP) state, as shown in (a) and (b), or a spiral-absorption (SA) state, as shown in (c), by the inclusion of Purkinje cells. The periodic time series in (g) and (h) and the regular peaks in the power spectra in (j) and (k) give additional evidence of the existence of such SRSP states in the endocardial layer with  $\mathcal{R} = 1$  and 2. The time series of  $V_e$  and  $V_p$  in (i) provides evidence for the disappearance of spiral waves in both the endocardial and Purkinje layers simultaneously at time  $t \simeq 5.7$  s for  $\mathcal{R} = 4$ .

We also focus on spiral-wave dynamics in the bilayer for the parameter sets  $\mathcal{P}2$  and  $\mathcal{P}3$  when an endocardial layer is coupled with a Purkinje layer with  $D_j$  and  $\mathcal{R}$  in the ranges mentioned above. With the  $\mathcal{P}2$  parameter set, we find that an SMST state in an isolated endocardial layer is converted to a single-rotating-spiral-periodic (SRSP) state, a single-rotating-spiral-quasiperiodic (SRSQ) state, a single-meandering-spiral-turbulence (SMST) state, a multiple-spiral-turbulence (MST) state, or a state with spiral-absorption (SA) by the inclusion of Purkinje cells. We find that the SRSP state, which we obtain for an isolated endocardial layer with the parameter set  $\mathcal{P}3$ , can lead to a transition to one of the above spiral states. We present below details of the spiral states in the endocardial layer of the bilayer with parameter sets  $\mathcal{P}1$ ,  $\mathcal{P}2$ , and  $\mathcal{P}3$ , and  $D_j$  and  $\mathcal{R}$  in the ranges mentioned above.

In Figs. 8(a)–8(c) we show, respectively, the various spiral states for the parameter sets  $\mathcal{P}1$ ,  $\mathcal{P}2$ , and  $\mathcal{P}3$ , as we vary (1) the normalized endocardial and Purkinje coupling parameters  $D_j^{\text{norm}}$  (i.e.,  $D_j^{\text{norm}} = D_j/D_{ee}$ ) and (2) the number of Purkinje-ventricular junctions, which we measure by  $\mathcal{R}$ .

Here circles (●), triangles (▲), diamonds (◆), pentagrams (★), and squares (■) represent, respectively, an SRSP, an SRSQ, an SMST, an MST, and an SA state. In the absence of the Purkinje-fiber layer, the endocardial layer displays an MST, an SMST, and an SRSP state, respectively, for the  $\mathcal{P}1$ ,  $\mathcal{P}2$ , and  $\mathcal{P}3$  parameter sets. These stability diagrams display the sensitive dependence of spiral-wave dynamics on (1) myocyte parameters (in terms of parameter sets  $\mathcal{P}1$ ,  $\mathcal{P}2$ , and  $\mathcal{P}3$ ), (2) the endocardial and Purkinje coupling parameters  $D_j$ , and (3) the number of Purkinje-ventricular junctions, which we measure by  $\mathcal{R}$ . Such sensitive dependence of the dynamics on system parameters arises from the underlying spatiotemporal chaos in the partial-differential-equation model that we use for cardiac tissue.

#### IV. DISCUSSION AND CONCLUSIONS

Our study is the first one that uses human ionic models of ventricular and Purkinje cells. This is important because, in human tissue, the action-potential duration in the Purkinje

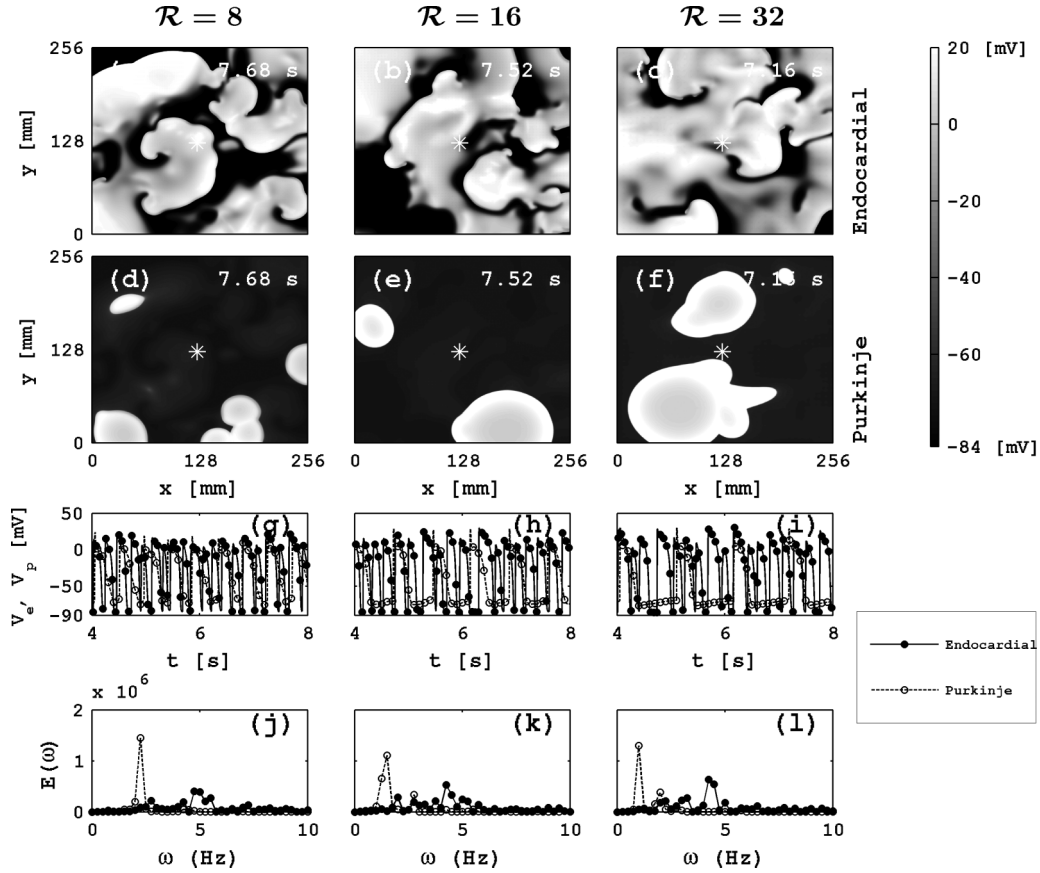


FIG. 7. Spiral-wave dynamics in our composite bilayer for the  $\mathcal{P}1$  parameter set for the endocardial cells with  $D_j = 0.1D_{ee}$  and  $\mathcal{R} = 8$  (left column),  $\mathcal{R} = 16$  (middle column), and  $\mathcal{R} = 32$  (right column); this figure is the analog of Fig. 6. An MST state in an isolated endocardial layer [Fig. 5(a)] still remains in the MST state on the inclusion of Purkinje cells, as shown by the pseudocolor plots of  $V_e$  in (a)–(c). The irregular time series obtained from a representative point in the endocardial layer [marked by asterisks in (a) to (f)] in (g)–(i) (●) and the broad-band power spectra of such time series in (j)–(l) (●) confirm the existence of such MST states in the endocardial layer of our composite bilayer. However, the Purkinje layer in the composite bilayer shows focal-wave activations as shown in the pseudocolor plots of  $V_p$  in (d)–(f); such focal-wave activity occurs periodically as shown by the time-series plots in (g)–(i) (○); and the focal-wave frequency decreases as  $\mathcal{R}$  increases, as shown by the power spectra in (j)–(l) (○).

network is almost the same as Ref. [30] or even shorter than that in the ventricular cells; this is different from, e.g., the rabbit cells used in Behradfar *et al.* [31], and the canine cells used in Cherry *et al.* [32], where the action potential in the Purkinje network is significantly longer than that in the myocardium.

We have coupled a Purkinje cell to an endocardial cell to study the morphology of the AP of both cells as investigated by Huelsing *et al.* [10,11]. Huelsing *et al.* have coupled *in vitro* a rabbit Purkinje cell to a ventricular myocyte by an electronic circuit. Our results on the delays in endocardial and Purkinje cells are in qualitative agreement with those of Refs. [10,23]. In particular, we have found that the delays are small if we apply a stimulus to the endocardial cell, and much longer if we apply it to the Purkinje cell. Such a delay increases as we decrease the diffusive coupling and eventually a failure of transmission occurs. Our studies have also revealed that the slope of the action-potential-duration-restitution curve of an endocardial cell can be lowered by coupling it with a Purkinje cell.

We use a simple regular Purkinje network compared to the detailed models of Refs. [31–34]. The simplicity of our minimal model for the Purkinje system has enabled us to study

in detail various types of wave dynamics over a wide range of coupling strengths and junction densities. Such a study has not been carried out so far. Therefore, our results complement those that have been obtained with realistic models.

The effects of such a regular network have also been used in the context of neural-network systems to study electrical-wave activation [35–37]. In particular, recent studies by Ma *et al.* [37] have used a two-dimensional square array with nearest-neighbor interactions to study defect-induced electrical-wave propagation in a neural network.

Bordas *et al.* [34] have carried out numerical simulations of electrical activation in ventricles, with a realistic, free-running, Purkinje-network system and the bundle of His, and a rabbit-ventricular-model in an anatomically detailed geometry, obtained from a high-resolution, magnetic-resonance data set. These authors have shown that the inclusion of the Purkinje system results in slightly faster and more coordinated activation of the ventricles than in a simple, ventricular model. Our studies produce similar results: multiple-spiral-turbulence and meandering-spiral-turbulence states disappear when we couple the Purkinje and endocardial layers with a high density



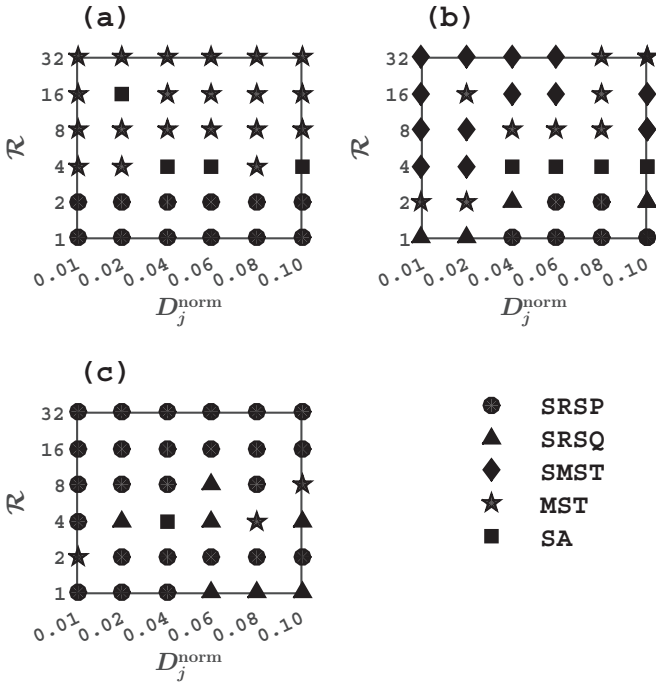


FIG. 8. The dependence of spiral-wave dynamics on (i) myocyte parameters, (ii) normalized endocardial and Purkinje coupling parameters  $D_j^{\text{norm}}$  (i.e.,  $D_j^{\text{norm}} = D_j/D_{ec}$ ), and (iii) the number of Purkinje-ventricular junctions, which we measure by  $\mathcal{R}$ . (a) This stability diagram displays various spiral states in the  $D_j^{\text{norm}}$  and  $\mathcal{R}$  parameter space for the  $\mathcal{P}1$  myocyte parameters; circles (●), triangles (▲), diamonds (◆), pentagrams (★), and squares (■) represent, respectively, a single-rotating-spiral-periodic (SRSP) state, a single-rotating-spiral-quasiperiodic (SRSQ) state, a single-meandering-spiral-turbulence (SMST) state, a multiple-spiral-turbulence (MST) state, and a state with spiral-absorption (SA); in the absence of the Purkinje-fiber layer, the endocardial layer displays an MST state. Panels (b) and (c) are the exact analogs of (a), but for the  $\mathcal{P}2$  and  $\mathcal{P}3$  parameter sets, respectively, for endocardial cells. An isolated endocardial layer displays SMST and SRSP states, respectively, for the  $\mathcal{P}1$  and  $\mathcal{P}2$  parameter sets.

of junctions (low values of  $\mathcal{R}$ ; see Figs. 6 and 8). Cherry *et al.* [32] have investigated electrical-wave propagation in a 2D canine ventricular tissue model coupled with a Purkinje system. Their study has shown that the Purkinje network can either terminate or promote wave breakup. Our studies have shown that the Purkinje layer can eliminate spiral waves in both endocardial and Purkinje layers depending on the initial conditions and interlayer coupling strength and density (Fig. 8). In addition, we observe focal waves, in the Purkinje layer, that enhance spiral-wave dynamics in the endocardial layer.

Studies by Behradfar *et al.* [31] have used a fractal method to develop a Purkinje-fiber network in an anatomically realistic rabbit-ventricular model with a biophysically realistic description of ion-channel dynamics and a bidomain model. This study has been motivated by the experimental study of ablation on the Purkinje network and its effect on the dynamics of ventricular fibrillation [38]. The authors have investigated the effects of the Purkinje-myocardium coupling strength and the Purkinje-ventricular junction density on reentry dynamics

in their model. They have observed that, for large junctional resistances, an increase in the Purkinje-ventricular junction density increases the mean firing rate in the Purkinje system, the fraction of successful retrograde conduction at Purkinje-ventricular junctions, and the incidence of wave break on the epicardium; but the mean firing of the ventricles is unchanged. Clear trends do not emerge if the junctional resistances are low. Our studies show that the firing rate of the Purkinje layer of the bilayer increased as the density of junctions is increased (Fig. 7); this is consistent with the studies by Behradfar *et al.* [31]. However, the probability of spiral breakup in the endocardial layer of a composite bilayer decreases as we increase the density of junctions (Fig. 8). This can be explained by analyzing the plots in Fig. 4, where we observe that the slope of the action-potential-duration-restitution plots of an endocardial cell, in a composite, decreases as the junctional strength increases. There is an additional decrease when we increase the density of junctions between Purkinje and endocardial layers. Therefore, we do not observe spiral breakup for high densities of junctions.

Our observations from our numerical studies are consistent with *in vitro* studies [38–40]. For example, Arnar *et al.* [39] have studied the origin of focal electrical activities that lead to ventricular tachycardia, in canine cardiac tissue, by using an activation-mapping technique. They have shown that in more than 60% of the cases of such ventricular tachycardia originate from the Purkinje-fiber system. In most cases, we find that the spiral waves in the endocardial layer change significantly when the endocardial layer is coupled to the Purkinje network. Studies by Tabereaux *et al.* [40] have shown that electrical activation can appear focally in the endocardial layer of a canine heart because of autorhythmic activities in the Purkinje system; such focal activation in the endocardial layer may help to produce abnormal or trigger activities, which can maintain preexisting ventricular fibrillation in the ventricular myocardium. In our composite-bilayer studies, we also observe autorhythmic excitation in the Purkinje layer for low densities of junctions (Fig. 7); and these excitations also disturb wave patterns in the endocardial layer.

The methods of nonlinear dynamics that we use help us to elucidate the spatiotemporal evolution of wave activation in our model for endocardial and Purkinje-fiber layers. In particular, we find sensitive dependence of spiral-wave dynamics on myocyte cell parameters and Purkinje-myocyte coupling conditions, in terms of both the diffusive coupling and the spatial distribution of Purkinje-ventricular junctions (see Fig. 8). Such sensitive dependence of the dynamics on system parameters is a signature of spatiotemporal chaos [6,41]; this sensitive dependence has not been explored hitherto in any mathematical model with coupled Purkinje fibers and myocytes in cardiac tissue. Furthermore, our study highlights the challenging, nonlinear-dynamics problems that can be found in cardiac-tissue models, whose study is of direct relevance to life-threatening cardiac arrhythmias. The detailed application of the methods of nonlinear dynamics to myocyte-Purkinje fiber systems, which we have presented here, can be extended to realistic models for cardiac tissue with, e.g., bidomain models [42,43], muscle-fiber orientation [44,45], and anatomical realistic simulation domains [46,47].

In our spiral-wave studies, we have used a square simulation domain whose linear size is larger than that of a typical human heart. Such a large simulation domain is required, as used in other studies [6,12], to avoid the frequent termination of spiral waves by collisions with the boundaries of the simulation domain. However, a domain of size comparable to a typical human heart can be used to get the same qualitative dynamics, but then only by using a scaling factor as suggested in Refs. [48–51].

## ACKNOWLEDGMENTS

We thank the Council for Scientific and Industrial Research (CSIR), Department of Science and Technology (DST), and University Grants Commission (UGC), India, and the Robert Bosch Centre for Cyber Physical Systems (IISc) for support, and the Supercomputer Education and Research Centre (SERC, IISc) for computational resources. A.V.P. and R.P. acknowledge support under the Utrecht-Asia Visiting Professor Programme of the University of Utrecht.

- 
- [1] A. Zaikin and A. Zhabotinsky, *Nature (London)* **225**, 535 (1970).  
 [2] K. Agladze, V. Krinsky, and A. Pertsov, *Nature (London)* **308**, 834 (1984).  
 [3] M. Bär, N. Gottschalk, M. Eiswirth, and G. Ertl, *J. Chem. Phys.* **100**, 1202 (1994).  
 [4] A. Pande and R. Pandit, *Phys. Rev. E* **61**, 6448 (2000).  
 [5] R. R. Aliev and A. V. Panfilov, *Chaos Solitons Fractals* **7**, 293 (1996).  
 [6] T. Shajahan, A. R. Nayak, and R. Pandit, *PLoS One* **4**, e4738 (2009).  
 [7] R. A. Gray, A. M. Pertsov, and J. Jalife, *Nature (London)* **392**, 75 (1998).  
 [8] J. Jalife, R. A. Gray, G. E. Morley, and J. M. Davidenko, *Chaos* **8**, 79 (1998).  
 [9] M. E. Mangoni and J. Nargeot, *Physiol. Rev.* **88**, 919 (2008).  
 [10] D. J. Huelsing, K. W. Spitzer, J. M. Cordeiro, and A. E. Pollard, *Am. J. Physiol.-Heart Circ. Physiol.* **274**, H1163 (1998).  
 [11] D. J. Huelsing, K. W. Spitzer, J. M. Cordeiro, and A. E. Pollard, *Am. J. Physiol.-Heart Circ. Physiol.* **276**, H572 (1999).  
 [12] K. Ten Tusscher and A. Panfilov, *Am. J. Physiol.-Heart Circ. Physiol.* **291**, H1088 (2006).  
 [13] P. Stewart, O. V. Aslanidi, D. Noble, P. J. Noble, M. R. Boyett, and H. Zhang, *Phil. Trans. R. Soc. A* **367**, 2225 (2009).  
 [14] P. W. Oosthoek, S. Viragh, W. Lamers, and A. Moorman, *Circ. Res.* **73**, 482 (1993).  
 [15] J. Tranum-Jensen, A. Wilde, J. Vermeulen, and M. Janse, *Circ. Res.* **69**, 429 (1991).  
 [16] A. V. Panfilov, *Phys. Rev. Lett.* **88**, 118101 (2002).  
 [17] A. R. Nayak, T. Shajahan, A. Panfilov, and R. Pandit, *PLoS One* **8**, e72950 (2013).  
 [18] H. Sun, N. Leblanc, and S. Nattel, *Am. J. Physiol.-Heart Circ. Physiol.* **272**, H1625 (1997).  
 [19] J. J. Mackrill, *Biochem. Pharmacol.* **79**, 1535 (2010).  
 [20] I. Schafferhofer-Steltzer, E. Hofer, D. J. Huelsing, S. P. Bishop, and A. E. Pollard, *IEEE Trans. Biomed. Eng.* **52**, 1522 (2005).  
 [21] A. R. Nayak and R. Pandit, *Front. Physiol.* **5**, 207 (2014).  
 [22] C. Porth, *Essentials of Pathophysiology: Concepts of Altered Health States* (Lippincott Williams & Wilkins, Philadelphia, PA, 2011).  
 [23] K. Ten Tusscher and A. Panfilov, *Prog. Biophys. Mol. Biol.* **96**, 152 (2008).  
 [24] F. H. Fenton, E. M. Cherry, H. M. Hastings, and S. J. Evans, *Chaos* **12**, 852 (2002).  
 [25] A. Garfinkel, Y.-H. Kim, O. Voroshilovsky, Z. Qu, J. R. Kil, M.-H. Lee, H. S. Karagueuzian, J. N. Weiss, and P.-S. Chen, *Proc. Natl. Acad. Sci. USA* **97**, 6061 (2000).  
 [26] Z. Qu, J. N. Weiss, and A. Garfinkel, *Am. J. Physiol.-Heart Circ. Physiol.* **276**, H269 (1999).  
 [27] A. Karma, *Chaos* **4**, 461 (1994).  
 [28] D. Durrer, R. T. Van Dam, G. Freud, M. Janse, F. Meijler, and R. Arzbaecher, *Circulation* **41**, 899 (1970).  
 [29] R. E. Ideker, W. Kong, and S. Pogwizd, *Pacing Clin. Electrophysiol.* **32**, 283 (2009).  
 [30] F.-Y. Lee, J. Wei, J.-J. Wang, H.-W. Liu, T.-C. Shih, and C.-I. Lin, *J. Heart Lung Transplant.* **23**, 737 (2004).  
 [31] E. Behradfar, A. Nygren, and E. J. Vigmond, *PLoS One* **9**, e88000 (2014).  
 [32] E. M. Cherry and F. H. Fenton, *Nonlin. Dyn.* **68**, 365 (2012).  
 [33] O. V. Aslanidi, P. Stewart, M. R. Boyett, and H. Zhang, *Biophys. J.* **97**, 20 (2009).  
 [34] R. Bordas, K. Gillow, Q. Lou, I. Efimov, D. Gavaghan, P. Kohl, V. Grau, and B. Rodriguez, *Prog. Biophys. Mol. Biol.* **107**, 90 (2011).  
 [35] K. Arai, E. L. Keller, and J. A. Edelman, *Neural Netw.* **7**, 1115 (1994).  
 [36] S. E. Folias and P. C. Bressloff, *Phys. Rev. Lett.* **95**, 208107 (2005).  
 [37] J. Ma, Y. Xu, J. Tang, and C. Wang, *Comm. Nonlin. Sci. Numer. Simul.* **34**, 55 (2016).  
 [38] D. J. Dossall, P. B. Tabereaux, J. J. Kim, G. P. Walcott, J. M. Rogers, C. R. Killingsworth, J. Huang, P. G. Robertson, W. M. Smith, and R. E. Ideker, *Am. J. Physiol.-Heart Circ. Physiol.* **295**, H883 (2008).  
 [39] D. O. Arnar, J. R. Bullinga, and J. B. Martins, *Circulation* **96**, 2421 (1997).  
 [40] P. B. Tabereaux, G. P. Walcott, J. M. Rogers, J. Kim, D. J. Dossall, P. G. Robertson, C. R. Killingsworth, W. M. Smith, and R. E. Ideker, *Circulation* **116**, 1113 (2007).  
 [41] T. K. Shajahan, S. Sinha, and R. Pandit, *Phys. Rev. E* **75**, 011929 (2007).  
 [42] M. Potse, B. Dubé, J. Richer, A. Vinet, and R. M. Gulrajani, *IEEE Trans. Biomed. Eng.* **53**, 2425 (2006).  
 [43] Y. Bourgault and C. Pierre, INSMI hal:00545888 (2010).  
 [44] R. Majumder, A. R. Nayak, and R. Pandit, *PLoS One* **6**, e18052 (2011).  
 [45] R. Majumder, A. R. Nayak, and R. Pandit, *PLoS One* **7**, e45040 (2012).  
 [46] A. V. Panfilov and J. Keener, *Chaos Solitons Fractals* **5**, 681 (1995).  
 [47] N. A. Trayanova and B. M. Tice, *Drug Disc. Today: Dis. Models* **6**, 85 (2009).

- [48] S. F. Noujaim, O. Berenfeld, J. Kalifa, M. Cerrone, K. Nanthakumar, F. Atienza, J. Moreno, S. Mironov, and J. Jalife, *Proc. Natl. Acad. Sci. USA* **104**, 20985 (2007).
- [49] S. Alonso, M. Bär, and B. Echebarria, *Rep. Prog. Phys.* **79**, 096601 (2016).
- [50] A. V. Panfilov, *Heart Rhythm* **3**, 862 (2006).
- [51] K. H. Ten Tusscher, A. Mourad, M. Nash, R. H. Clayton, C. P. Bradley, D. J. Paterson, R. Hren, M. Hayward, A. V. Panfilov, and P. Taggart, *Exp. Physiol.* **94**, 553 (2009).